J. Astrophys. Astr. (2023) 44:77
https://doi.org/10.1007/s12036-023-09968-2

PRE-MAIN SEQUENCE STARS

Protoplanetary disks around young stellar and substellar objects in the σ Orionis cluster

BELINDA DAMIAN[1,*], JESSY JOSE[2], BETH BILLER[3,4] and K. T. PAUL[1]

[1]Department of Physics and Electronics, CHRIST (Deemed to be University), Hosur Road, Bengaluru 560029, India.
[2]Indian Institute of Science Education and Research (IISER) Tirupati, Rami Reddy Nagar, Karakambadi Road, Mangalam (P.O.), Tirupati 517507, India.
[3]SUPA, Institute for Astronomy, University of Edinburgh, Blackford Hill, Edinburgh EH9 3HJ, UK.
[4]Centre for Exoplanet Science, University of Edinburgh, Edinburgh, UK.
*Corresponding author. E-mail: belinda.damian@res.christuniversity.in

MS received 3 November 2022; accepted 29 May 2023

Abstract. Understanding the evolution and dissipation of protoplanetary disks are crucial in star and planet formation studies. We report the protoplanetary disk population in the nearby young σ Orionis cluster ($d \sim 408$ pc; age $\sim$ 1.8 Myr) and analyse the disk properties, such as dependence on stellar mass and disk evolution. We utilize the comprehensive census of 170 spectroscopic members of the region refined using astrometry from Gaia DR3 for a wide mass range of $\sim$19–0.004 $M_{\odot}$. Using the near-infrared (2MASS) and mid-infrared (WISE) photometries, we classify the sources based on the spectral index, into class I, class II, flat spectrum and class III young stellar objects. The frequency of sources hosting a disk with stellar mass $<2\ M_{\odot}$ in this region is 41 ± 7%, which is consistent with the disk fraction estimated in previous studies. We see that there is no significant dependence of disk fraction on stellar mass among T Tauri stars ($<2\ M_{\odot}$), but we propose rapid disk depletion around higher mass stars ($>2\ M_{\odot}$). Furthermore, we found the lowest mass of a disk-bearing object to be $\sim$20 M_{Jup} and the pronounced disk-fraction among the brown dwarf population hints at the formation scenario that brown dwarfs form similar to low-mass stars.

Keywords. Star forming regions—protoplanetary disks—young stellar objects.

1. Introduction

In the star formation scenario, circumstellar disks form around protostars as a consequence of the conservation of angular momentum (Andre *et al.* 2000; Williams & Cieza 2011). The presence of these disks have been evidenced through observational studies of the accretion signatures and infrared excess emission due to the dusty disk. As the system evolves, the disk dissipates through: (i) accretion on to the central protostar channeled by the magnetic field lines from the inner edge of the disk to the stellar surface (see reviews by Bouvier *et al.* 2007; Hartmann *et al.* 2016), (ii) accumulation into planets (see review by Miotello *et al.* 2022), (iii) photo-evaporation due to the radiation from the protostar (see reviews by Frank *et al.* 2014; Pascucci *et al.* 2022) and (iv) external photo-evaporation due to nearby massive stars (Hartmann 2009; Winter *et al.* 2018). The optically thick inner disk present during the early phases of disk evolution produces excess over the stellar photosphere that can be detected by studying the young stellar objects (YSOs) in the near-infrared (NIR) and mid-infrared (MIR) wavelengths (Hartigan *et al.* 1995).

The lifetime of the disk depends on the disk dissipation timescale. This has a direct effect on the planet formation since the circumstellar disks are the birth sites for planets and provide raw materials for its formation. Hence, they impact when and what type of planets can form (Meyer *et al.* 2007; Currie *et al.* 2009). Previous studies have shown that timescale for the disk evolution is dependent on the stellar mass (Lada & Lada 1995; Calvet *et al.* 2004). The disk frequency around massive

---

This article is part of the Special Issue on "Star formation studies in the context of NIR instruments on 3.6 m DOT".

stars ($>1\ M_{\odot}$) has been observationally reported to be lower than that in low-mass stars, which implies a rapid disk dispersal in early-type stars (Lada *et al.* 2006; Dahm & Hillenbrand 2007; Hernández *et al.* 2007).

Due to the dependence of disk fraction on stellar mass, the time available for the formation of planets around early-type stars is low. However since the disk mass is relative to the stellar mass, there is a higher possibility to encounter giant planets in the vicinity of massive stars (Johnson *et al.* 2010). Hence, quantifying the disk frequency as a function of stellar mass and age is essential to understand the disk lifetime and in turn constrain the planet-formation theories (Andrews 2020; Rilinger & Espaillat 2021).

The σ Orionis cluster located near the Horsehead nebula below the Orion belt in the Ori OB1b association is one of the well-studied regions in the Orion complex. Due to its proximity ($d \sim 408$ pc; Damian *et al.* 2023) and low extinction ($A_{\rm V} \sim 0.4$ mag; Damian *et al.* 2023), we have a strong census of the sources in the region including the very low-mass objects. Also due to its youth (∼2 Myr; Damian *et al.* 2023), this is an ideal target to study the disk properties of young stars in their primordial stages of evolution. Having a robust catalog of spectroscopically confirmed members in the core of the region, we study the disk properties, such as disk frequency and its dependence on stellar mass and age.

This paper is organized as follows: Section 2 describes the data used in this work, Section 3 discusses the selection of members of the region and Section 4 presents estimation of physical parameters of the members. In Section 5, we classify the members based on the IR SED slope into different evolutionary stages of YSOs and in Section 6, we estimate the disk fraction and discuss its dependence on stellar mass as well as disk evolution. Section 7 summarizes the results of this work.

2. Data

The primary data set of the members of the σ Orionis cluster is taken from Damian *et al.* (2023). In Damian *et al.* (2023), NIR photometry from the Wide-field InfraRed Camera (WIRCam) on the Canada–France–Hawaii Telescope (CFHT) (Puget *et al.* 2004) in J-, H- and W-bands for a survey area of ∼21 × 21 arcmin centered at RA $= 84.700°$ and Dec $= -2.568°$ is used. Along with this, to classify the YSOs and to characterize the disk-bearing members of the region, we use the NIR and MIR data from the Two Micron All Sky Survey (2MASS) (Cutri *et al.* 2003) and Spitzer (Spitzer Science Center (SSC) & Infrared Science Archive (IRSA) 2021)/Wide-field Infrared Survey Explorer (WISE) (Cutri *et al.* 2012), respectively. The CFHT WIRCam data is used as the base catalog and we found counterparts for those sources with a cross-match radius of 1 arcsec in 2MASS (J, H and $K_{\rm s}$), Spitzer (IRAC 3.6, 4.5, 5.8 and 8 μm) and WISE (W1 (3.4 μm), W2 (4.6 μm), W3 (12 μm) and W4 (22 μm)).

3. Membership selection

We use the catalog of 170 spectroscopically confirmed members of the σ Orionis region from Damian *et al.* (2023). The selection and compilation of the members are briefly described below. The members compiled in Damian *et al.* (2023) comprise of newly confirmed sources as well as known members in literature. First, we identified the brown dwarf candidates using the CFHT WIRCam data based on the reddening insensitive index (Q), which is defined as follows:

$$Q = (\mathrm{J} - \mathrm{W}) + e(\mathrm{H} - \mathrm{W}), \tag{1}$$

where J, H and W are the magnitudes from the corresponding filters and e is the ratio of extinction in each of these bands. The Q index is defined to identify brown dwarfs in star-forming regions and distinguish them from foreground and background field stars independent of reddening (refer Allers & Liu 2020). The value of Q is scaled such that $Q = 0$ corresponds to $M0$ type objects, which do not show significant water absorption feature and decreasing values of Q correspond to objects of later spectral types (for instance $Q = -0.6$ relates to M6 type object (∼0.08 $M_{\odot}$)), which show prominent water absorption in their atmosphere. The selection criteria $Q < -(0.6 + 3\sigma_Q)$ is used to select the candidate i.e., very low-mass stars and brown dwarfs in the region, where the uncertainty in $Q(\sigma_Q)$ is estimated by propagating the errors in J, H and W (see Jose *et al.* 2020 for details).

Second, the candidates were selected using the Gaia DR3 (Gaia Collaboration 2022) photometric and astrometric data. We incorporate the following astrometric quality conditions: renormalized unit weight error (RUWE) <1.4, which filters the sources with unreliable astrometric solutions (Fabricius *et al.* 2021; Manara *et al.* 2021; Das *et al.* 2023; Kordopatis *et al.* 2023; Stoop *et al.* 2023) and $\sigma_\pi/\pi < 0.1$, where π is parallax and σ_π is the uncertainty in parallax (Esplin & Luhman 2022; Penoyre *et al.* 2022). Sources satisfying the above conditions and located along the pre-main sequence (PMS) branch in the $\mathrm{Gaia_G}$–J vs absolute $\mathrm{Gaia_G}$ color magnitude diagram (CMD) with parallax and proper motion consistent with that of the cluster are selected as candidate members. These astrometric conditions are applied to known members of the region in literature as well, to filter sources, which have astrometry inconsistent with that of the cluster (refer Damian *et al.* 2023 for more details).

Together we identified 28 low-mass stars and brown dwarf candidates and obtained their spectra with the 3.2-m NASA Infrared Telescope Facility (IRTF) SpeX (Rayner *et al.* 2003). The observations were carried out in the low-resolution prism mode ($R \sim 150$) covering the wavelength range of 0.7–2.5 μm. Along with these newly identified members, the previously known members of the σ Orionis cluster within the CFHT survey area ($\sim 21 \times 21$ arcmin) were combined comprising of 170 spectroscopically confirmed members including the massive O9.5 star (σ Ori) down to the planetary mass sources. The complete catalog of members is adopted as it is from Damian *et al.* (2023) for this work. The data is complete, down to $\sim 0.004\ M_\odot$ in all the three CFHT WIRCam J-, H- and W-bands.

4. Physical parameters of members

Parameters of the members of the region like spectral type, effective temperature ($T_{\rm eff}$), bolometric luminosity and mass estimated in Damian *et al.* (2023) are incorporated in this work. The spectral types for the previously known members are adopted from literature and for the newly identified low-mass sources in Damian *et al.* (2023) are obtained through comparison of the IRTF NIR spectra with standard spectral templates. The spectral types for the 170 members range from O9.5 for the massive star σ Ori at the center of the cluster to L5 for the lowest planetary mass source. $T_{\rm eff}$ is obtained from the spectral type using the appropriate relations from Pecaut & Mamajek (2013) (for O9.5–M5 type), Herczeg & Hillenbrand (2014) (for M5.5–M6.5 type) and Filippazzo *et al.* (2015) (for M7–L5 type). Then, the bolometric luminosity for the massive O, B and A type sources are incorporated based on their spectral type from the extended table of Pecaut & Mamajek (2013). Whereas for the other spectral type sources, it is derived from the bolometric magnitude incorporating the bolometric correction (BC) given by the following equation:

$$\log\left(\frac{L_{\rm bol}}{L_\odot}\right) = -\frac{(M_{\rm bol} - M_{\rm bol,\odot})}{2.5}, \qquad (2)$$

where $M_{\rm bol} = m_{\rm J} - 5\log(d) + 5 - A_{\rm J} + BC_{\rm J}$ and distance to the region is estimated to be 408 ± 8 pc based on Gaia DR3 parallax; the mean extinction towards the cluster $A_v = 0.4$ mag and the solar bolometric magnitude $M_{\rm bol,\odot} = 4.73$ mag. Utilizing these $T_{\rm eff}$ and luminosity estimates, the mass of the sources are determined from the HR-diagram using the isochrones and evolutionary models of PMS stars from Baraffe *et al.* (2015) (for mass $>0.01\ M_\odot$) and the models from BT-Cond (Baraffe *et al.* 2003; for mass $<0.01\ M_\odot$). The average age of the cluster was estimated as 1.8 ± 1 Myr. Members list from Damian *et al.* (2023) along with their physical parameters are given in Appendix.

5. Classification of YSOs using spectral index

We classified the different evolutionary stages of the YSOs following the methodology described in Koenig *et al.* (2015). This can be quantified using the slope of the spectral energy distribution from NIR to MIR wavelengths (Lada 1987). Greene *et al.* (1994) classified the YSOs based on the value of the infrared spectral index (α), which reflects the slope of the SED, into four stages of evolution: Class I, class II, flat spectrum and class III. The slope α is expressed as:

$$\alpha = \frac{d\log(\lambda F_\lambda)}{d\log\lambda}. \qquad (3)$$

In the above equation, the wavelength (λ) and flux density (F_λ) are calculated using the zero-point for the respective filters taken from the VOSA filter profile service[1]. Here, we compute α with the dereddened 2MASS K_s ($\lambda = 2.1\ \mu$m) and WISE W4 ($\lambda = 22\ \mu$m) bands whenever possible. To deredden the data, we use the mean extinction towards the cluster $A_v = 0.4$ mag and the extinction relation from Cardelli *et al.* (1989) and Koenig & Leisawitz (2014) for the 2MASS and WISE magnitudes, respectively. We apply the condition that the uncertainty in K_s should be non-null with the SNR in W4 ≥ 5 and the reduced χ^2 of the W4 profile-fit photometry measurement ($\chi^2_{\rm W4}$) between 0.3 and 1.7 (Koenig *et al.* 2015). These conditions are satisfied by 34 sources, whose SED slope is estimated using the K_s and W4 wavelengths. When a source does not comply with the criteria for W4, then we use the W3 ($\lambda = 11.6\ \mu$m) band with the same condition for SNR and $\chi^2_{\rm W3}$, which is the case for 74 sources. When both W4 and W3 photometries do not satisfy the condition, we then resort to W2 ($\lambda = 4.6\ \mu$m) filter as for 35 sources. For these 35 sources, estimating α with H- instead of K-band photometry does not result in a significant

---

[1] http://svo2.cab.inta-csic.es/theory/fps/.

change in the YSO classification. In the case when K_s data is unavailable or with null photometric error then, the slope value is calculated between W1 (SNR $\geq$ 3) and W4 (SNR $\geq$ 5; $0.3 < \chi^2_{W4} < 1.7$) (Koenig *et al.* 2015). Twenty five sources either do not have WISE data or 2MASS data or their photometry do not meet the quality requirements. Therefore, we obtain the spectral index for 145 members of the region (see Appendix) and classify the sources as class I ($\alpha \geq 0.3$), flat spectrum ($0.3 > \alpha \geq -0.3$), class II ($-0.3 > \alpha \geq -1.6$) and class III ($\alpha < -1.6$) (Greene *et al.* 1994; Koenig *et al.* 2015).

Table 1 summarizes YSO class of members. Among the 145 sources that are classified into various YSO classes, the majority of the sources are identified as class III objects. Further analysis on the disk fraction and its significance are presented in Section 6.

In Figure 1, we show the color–color diagram with 2MASS and WISE highlighting the distribution of the disk and diskless sources. We see a distinct color excess for the class II sources indicating the presence of a circumstellar disk around them. The sources with negative MIR color excess (in W1–W2) are mainly the early type stars of O to A spectral class. Likewise in Figure 2, we show the 2MASS J–WISE W2 CMD for the sources observed with the WIRCam from Damian *et al.* (2023) as mentioned in Section 2. Here, we see that the class III objects are aligned along the PMS branch consistent with the 2 Myr isochrone (Baraffe *et al.* 2015), whereas the sources hosting the disk are to the right due to the NIR excess emission from its disk.

Table 1. Spectral index-based classification of the members of the σ Orionis cluster.

Class	α	Number of sources
I	$\geq$0.3	2
Flat spectrum	<0.3 and $\geq$−0.3	3
II	<−0.3 and $\geq$−1.6	54
III	<−1.6	86

Figure 3 shows the relation between the spectral type of the sources and the extinction corrected color. To deredden the 2MASS, WISE and Spitzer data, we adopt the mean extinction to the cluster $A_v = 0.4$ mag (Damian *et al.* 2023) and the reddening relation from Cardelli *et al.* (1989), Koenig & Leisawitz (2014) and Wang & Chen (2019), respectively. The continuous line marks the trend of the intrinsic photospheric color as a function of spectral type from Pecaut & Mamajek (2013) Table 6 for K_s – W2 color and from Esplin & Luhman (2017) for K_s – [8.0] color. We compare the colors of the sources classified as class II with the typical photospheric colors of YSOs for a given spectral type and we see that the dereddened K_s–[8.0] color shows an excess of >1 mag. Likewise in the top panel of Figure 3 the class II sources exhibit an excess in the dereddened K_s – W2 color than the corresponding photospheric sequence indicating that the excess is likely due to the presence of a circumstellar disk in the system. We also note from the distribution of disk bearing (class II) and

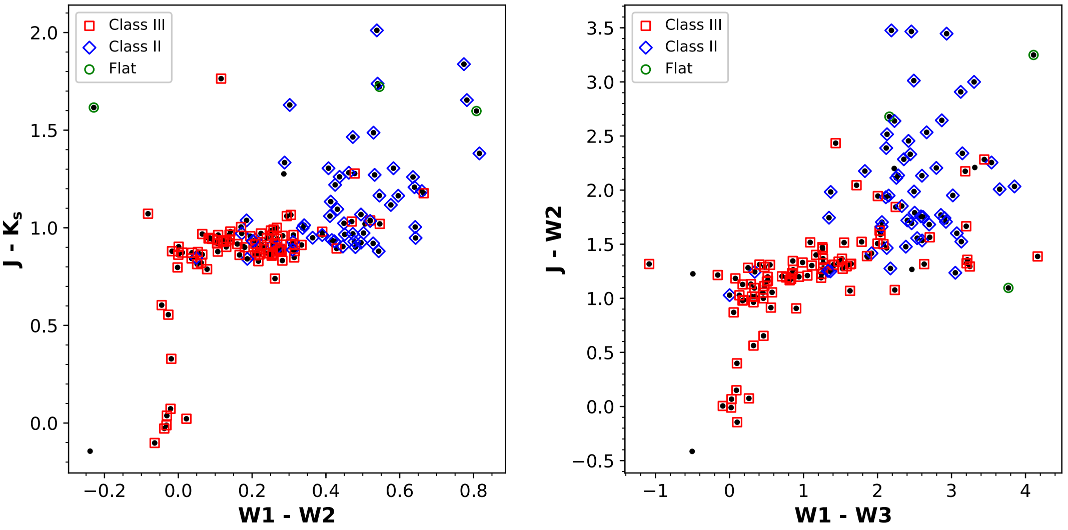

Figure 1. Left: WISE W1–W2 vs 2MASS J–K_s color–color diagram of the members of the σ Orionis cluster (black dots). The excess and non-excess sources classified using the SED slope (α) are marked with different colors as presented in the legend. Right: WISE W1–W3 vs 2MASS J–WISE W2 color–color diagram with the same color scheme as the left figure.

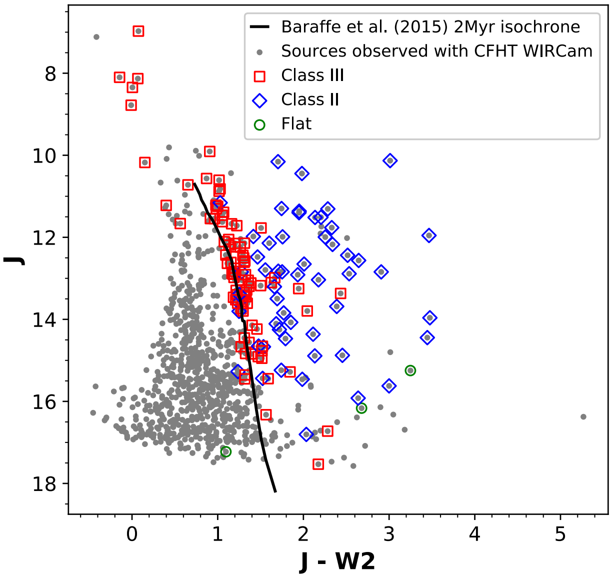

Figure 2. 2MASS J–WISE W2 vs J color–magnitude diagram. The markers represent the different types of YSOs as given in the legend. The black line shows the 2 Myr isochrone from Baraffe *et al.* (2015).

diskless sources (class III) in the figure that the color excess decreases towards the late M type objects relative to the excess seen in the early more massive sources possibly caused by the more massive disks around them.

6. Results and discussion

6.1 *Disk fraction*

We estimate the disk fraction of the σ Orionis cluster, which essentially gives the percentage of disk-bearing sources among members of the region. Here, we consider the sources identified as class II, class I and flat spectrum as disk-bearing sources and the disk fraction is calculated as the number of disk-bearing sources divided by the total number of sources. Since there are no disk sources among the massive members, we only consider sources with mass $<2\ M_\odot$ for the estimate. This yields a disk frequency of 41 ± 7% (error is estimated from Poisson uncertainty). Previous disk

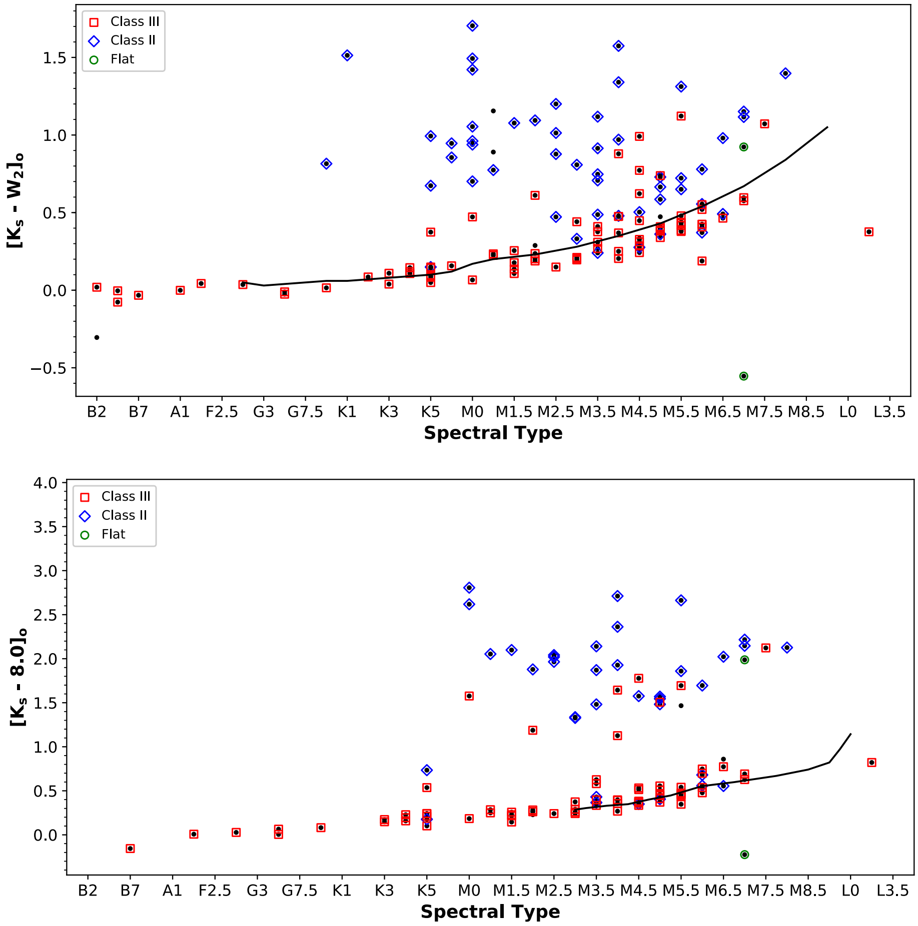

Figure 3. Spectral type as a function of extinction corrected K_s–W2 and K_s–[8.0] color. The markers represent different types of YSOs as given in the legend. The black line indicates the sequence of the intrinsic photospheric color of young stars taken from Pecaut & Mamajek (2013) (top panel) and Esplin & Luhman (2017) (bottom panel).

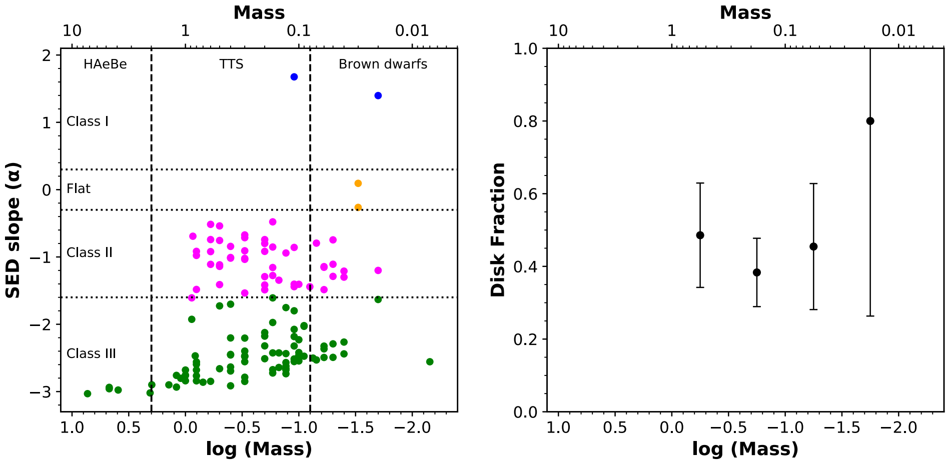

Figure 4. Left: Logarithmic stellar mass as a function of the SED slope estimated in Section 5. The vertical dashed lines denote the mass range of the Herbig AeBe stars, T Tauri stars and brown dwarfs. The horizontal dotted lines mark the range of the α values for each YSO class. Right: Disk fraction for every logarithmic mass bin of size 0.5 dex. The error bars denote the Poisson error at each point.

studies on this region based on the Spitzer IRAC color excess have quoted similar results and some of them are reported below. Hernández *et al.* (2007) reported that the disk fraction depends on the stellar mass ranging from ∼10% for HAebe stars to ∼35% for T Tauri stars. Luhman *et al.* (2008) estimated the disk frequency for low-mass stars as ∼40% and for the brown dwarfs as ∼60%. Later, Peña Ramírez *et al.* (2012) derived a similar result of ∼40% for the very low-mass stars, brown dwarfs and planetary-mass objects. These previous studies on the σ Orionis cluster have reported a disk fraction, which is consistent with our current estimate based on a comprehensive membership of spectroscopic members down to the planetary mass regime in the core of the region.

6.2 *Dependence of disk fraction on stellar mass*

With the estimated disk fraction, we obtained its correlation and dependence on the stellar mass as shown in Figure 4. The confirmed members of the region were grouped together based on their mass into Herbig AeBe stars ($>2\ M_{\odot}$; Guzmán-Díaz *et al.* 2021), T Tauri stars (2–0.08 $M_{\odot}$; Furlan *et al.* 2006) and brown dwarfs ($<0.08\ M_{\odot}$; Luhman 2012). The left panel of Figure 4 shows the distribution of the various classes of objects in relation to their stellar mass and in the right panel, we chart the fraction of disk-bearing sources emitting IR excess for every logarithmic bin of 0.5 dex.

We see that there is no significant variation of disk fraction with respect to mass and the majority of the disk sources consist of T Tauri stars with a scarcity of excess sources towards the high mass end (mainly above 2 $M_{\odot}$). Although the disk fraction seems to increase in the lowest mass bin (i.e., the planetary mass objects); however, this must be treated with caution due to the high uncertainty in the disk fraction estimate and also since we do not classify 25 YSOs (refer Section 5), this could cause incompleteness in the data towards the low-mass end. The low disk frequency for stars with mass $>1\ M_{\odot}$ could be a signature of rapid disk evolution of the high mass stars, whereas for the low-mass stars with higher excess, this can be attributed to longer disk lifetime.

A similar case was reported in the nearby (∼300 pc) young (∼1–2 Myr) cluster NGC 1333 by Yao *et al.* (2018). Their scarce population of intermediate mass stars does not favor a robust comparison of disk fraction with the low-mass population. However, they estimate the disk fraction for the low-mass stars (0.1–1.5 $M_{\odot}$) to be consistent, lacking any significant variation with respect to mass. Yao *et al.* (2018) also analysed the dependence of disk fraction on stellar mass for the young star-forming region IC 348 (∼3 Myr; ∼320 pc). They found that the high mass region (2.2–5 $M_{\odot}$) hosts the lowest disk frequency and the disk frequency increases towards the low-mass stars (0.25–1.5 $M_{\odot}$).

Ribas *et al.* (2015) carried out a detailed study to test the influence of stellar mass on the protoplanetary disk evolution using a large sample of spectroscopically confirmed YSOs (∼1400) in 22 nearby associations (<500 pc) spread across different ages of ∼1–100 Myr. They grouped the sample into two based on stellar mass with a boundary mass of 2 $M_{\odot}$. They found robust evidence for dependence of disk lifetime on stellar mass, where the high mass stars were found to disperse their disks

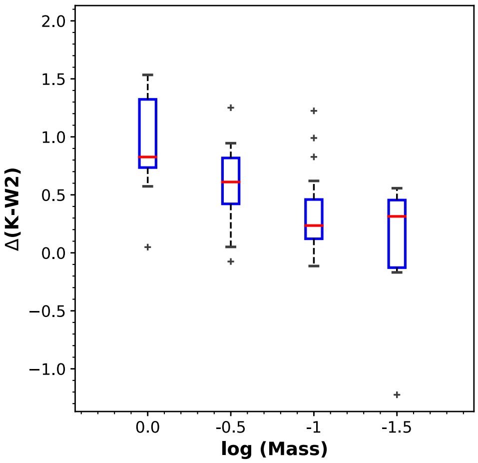

Figure 5. Box and whisker plot between mass and color excess of YSOs with disk in the σ Orionis cluster. The box marks the lower (Q1) and upper (Q3) quartile range and the red horizontal line denotes the median for a bin of size 0.5 dex (width of the box has no significance here). The whisker extends from 5th to 95th percentile and the outliers are marked with the plus symbol.

rapidly, twice as quickly as low mass stars. This is due to the lower efficiency of the mechanisms responsible for removing circumstellar gas and dust around low mass stars leading to longer timescales for planet formation around such hosts. This is in agreement with our observations of disk dispersal in the σ Orionis cluster between T Tauri and Herbig AeBe stars.

6.3 *Analysis on NIR excess*

The three major contributing factors for the observed color of the YSOs are the photospheric color, the circumstellar excess and interstellar reddening. To determine the NIR excess due to the presence of disk, we follow the definition proposed in Hillenbrand *et al.* (1998) as given in the below equation. We use the 2MASS K-band and WISE W2 magnitudes to obtain the excess:

$$\Delta(\text{K–W2}) = (\text{K–W2})_{\text{o}} - (\text{K–W2})_{\text{phot}}, \tag{4}$$

where $(\text{K} - \text{W2})_{\text{o}}$ is the extinction corrected observed color and $(\text{K} - \text{W2})_{\text{phot}}$ is the intrinsic photospheric color. The extinction $A_v = 0.4$ mag is adopted from Damian *et al.* (2023) and we use the reddening relation from Cardelli *et al.* (1989) and Koenig & Leisawitz (2014) to obtain extinction in K- and W2-bands, respectively. The $(\text{K} - \text{W2})_{\text{phot}}$ as a function of spectral type is taken from Pecaut & Mamajek (2013). In Figure 5, we present the distribution of NIR excess for the disk-bearing sources (class I, class II and flat spectrum sources) identified in Section 5. Although we see a slight decline in the NIR excess as we move towards the very low-mass end, we cannot conclusively deduce the dependence of disk excess on the stellar mass due to two caveats—scarcity of high mass sources harboring disk mainly above 1 $M_{\odot}$ and the low number density of such sources in the region resulting in a high uncertainty in the estimated NIR color excess. Yao *et al.* (2018) analysed the NIR excess of sources hosting disk around them in the Orion A molecular cloud using 2MASS K-band and Spitzer 4.5 μm color. They found that the excess decreases for stars between the mass range of 0.36 and 0.42 $M_{\odot}$.

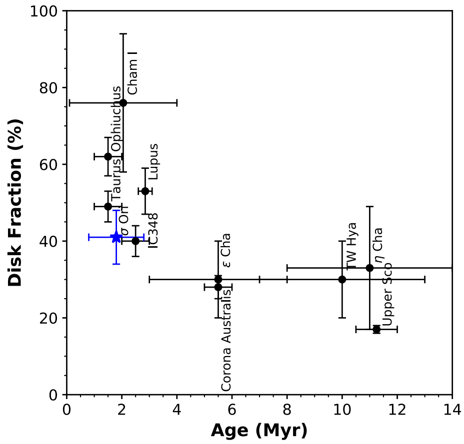

Figure 6. Age as a function of disk fraction in different star-forming regions. The data points for Ophiuchus, Taurus, Cham I, IC348, Lupus, ϵ Cha, Corona Australis, TW Hydra, η Cha and Upper Scorpius are taken from Michel *et al.* (2021) with their respective errors. The disk fraction of the σ Orionis cluster estimated in this work is shown with the blue star and the error bar denotes the Poisson error.

6.4 *Disk evolution*

The gas and dust in the protoplanetary disks are the building blocks for planets. Therefore, the frequency and dispersal of disks around stars of different ages is important to constrain planet formation theories.

Figure 6 shows the relation between the disk fraction and the age of various young star-forming regions from literature along with the relation for the σ Orionis cluster reported in this work. In Damian *et al.* (2023), the mean age of the cluster is computed as the average age of the confirmed members of the region from the HR-diagram as 1.8 ± 1 Myr. The disk fraction and age of other star-forming regions are adopted from Michel *et al.* (2021) (Table 1), where the disk fraction is estimated based on the the SED slope (α_{Lada}) between 2 and 22 μm (i.e., 2MASS K–WISE4), which is similar to the wavelengths that we have utilized for σ

Orionis to estimate the disk fraction and α range for YSO classification. The age of the star-forming regions range between 1 and 12 Myr with decreasing disk frequency for older regions. We see that our estimate for the σ Orionis cluster of 41% at 1.8 Myr matches with the trend of other star-forming regions (Panwar *et al.* 2017; Das *et al.* 2021; Gupta *et al.* 2021).

Among the various mechanisms contributing to the dispersion of protoplanetary disks, the two external factors that affect disk lifetime are external photo-evaporation due to the ultraviolet (UV) flux from massive stars in the vicinity and due to tidal truncation caused by close encounters. Winter *et al.* (2018) quantified the threshold for a system to be under the influence of these two mechanisms by measuring the far-UV (FUV) flux driving the external photo-evaporation and the stellar number density attributed to the tidal truncation for star-forming regions under varying local environments. They derived a threshold for the number density to be $>10^4$ pc^{-3} for a period of 3 Myr above which the effect of tidal truncation is significant in disk dispersion. Additionally for the host star of $\sim 1\ M_\odot$ with a massive disk around it, $\sim 0.1\ M_\odot$ the minimum FUV flux required to dissipate the disk within 3 Myr is $G_o > 3000$ (where G_o is the FUV flux of the interstellar). The number density and the FUV flux in the σ Orionis cluster is below the minimum values reported in Winter *et al.* (2018) for the system to be influenced by external photo-evaporation and tidal truncation (refer Figure 3 of Winter *et al.* 2018). On the other hand, Ansdell *et al.* (2017) surveyed the gas and dust in disks around YSOs in the region using ALMA and found a decline in the disk dust mass at smaller separations from the central massive star (σ Ori). They claim that the external photo-evaporation influences disk evolution in the region. However, as the latter study probes mainly the outer part of the disk, which could explain the discrepancy. Therefore, we cannot conclusively rule out the effect of external photo-evaporation on disk evolution in this region and our robust sample of members can facilitate in refining further works in this regard.

6.5 *Disks around brown dwarfs and planetary mass objects*

The formation scenario of brown dwarfs and planetary mass objects ($<0.08\ M_\odot$) is still an open question. Various mechanisms have been proposed to explain the formation of these substellar objects, such as turbulent fragmentation—the compression of gas in the molecular cloud forms cores, which collapses into low mass objects (Padoan & Nordlund 2002; Andre *et al.* 2012); dynamical ejection—the core is ejected out of a multiple system before it could accrete enough mass to start hydrogen burning (Reipurth & Clarke 2001); photoerosion—the outer layers of a prestellar core are eroded by nearby massive stars before it accretes onto the central protostar (Whitworth & Zinnecker 2004); disk fragmentation—gravitational fragmentation of the disk material (Stamatellos *et al.* 2011; see review by Luhman 2012). Similar to newly formed stars, brown dwarfs have been observed to host a disk around them (Muench *et al.* 2001; Natta *et al.* 2002).

In young star-forming regions, it has been observed that the frequency of disks harbored by brown dwarfs are comparable with the disk fraction among stars (Luhman *et al.* 2005). The presence of disk around these substellar objects are indicative of their formation mechanism, which supports the theory that brown dwarfs form like stars. Additionally, observational studies have reported the presence of planetary mass companions hosted by brown dwarfs, analogs to planets around stars (Han *et al.* 2013; Shvartzvald *et al.* 2017). Protoplanetary disks contain raw materials and are the birth sites of planets. Therefore, understanding the evolution of disks is crucial in constraining the brown dwarf and planet formation theories (Rilinger & Espaillat 2021).

Another interesting question to investigate is whether these planetary mass objects can host their own planetary systems. Detecting signatures of disk around these objects would unravel their nature and shed light on their formation mechanism. However, it is challenging to observe these ultra cool objects due to their low luminosity and distinguish them from field contaminants. This requires deep imaging of significantly large areas of young star-forming regions for a statistically robust sample followed by spectroscopic confirmation of youth. A recent study by Scholz *et al.* (2023) using Spitzer photometry in 3.6 and 4.5 μm reported the lowest mass of an object harboring a disk in the NGC 1333 region to be $\sim 10\ M_{\mathrm{Jup}}$. They also reviewed various other nearby star-forming regions and found the results to be consistent. This may indicate that $\sim 10\ M_{\mathrm{Jup}}$ could be the lower limit for the opacity limited fragmentation to form like stars. With our deep photometry and W-band technique of identifying these ultra cool objects, along with the IR excess analysis using WISE data, we found that for the central region of the σ Orionis cluster, the lowest mass objects with a disk are $\sim 20\ M_{\mathrm{Jup}}$ (WBIS_053854.9-024033.8 and WBIS_053900.3-023705.9). WBIS_053900.3-023705.9 (UGCS J053900.29-023705.7) and WBIS_

053854.9-024033.8 (2MASS J05385492-0240337) are classified as class I and class II YSOs, respectively (refer Table 2).

In the σ Orionis cluster, we see a pronounced population of protoplanetary disks around brown dwarfs (refer Figure 4). Although the MIR data towards the very low mass end is incomplete, we see that among the 25 substellar sources ($<0.08\ M_{\odot}$) that were classified in Section 5, 14 sources harbor disks (class I + class II + flat spectrum), which give the upper limit of the disk fraction in this regime. Given that, we have used a robust sample of spectroscopically confirmed brown dwarfs in the region despite the lack of a large sample, the significant disk fraction in the substellar mass range cannot be overlooked. This non-negligible disk fraction among the brown dwarf population provides clues to its possible origin similar to that of low-mass stars formed via turbulent fragmentation of the molecular cloud.

7. Conclusions

Utilizing the comprehensive catalog of spectroscopic members in the nearby young σ Orionis cluster from Damian *et al*. (2023), we have analysed the protoplanetary disk properties of the YSOs. Our members have also been refined based on astrometry from Gaia DR3. We have used the 2MASS and WISE NIR photometries to classify the members based on the infrared spectral index into the four YSO classes—class I, class II, flat spectrum and class III. We then verified the presence of the disk around the YSOs by comparing their color excess with the intrinsic photospheric color for a given spectral type as well as their distribution in the NIR and MIR color–color diagrams. We see that the class II sources show a distinct color excess indicating that the excess is due to the presence of a circumstellar disk around the source. The disk frequency of the σ Orionis cluster was found to be 41±7% and this correlates well with the age of the cluster when compared with other star-forming regions.

We also analysed the dependence of disk fraction on stellar mass, which showed that there is no significant variation of disk frequency with respect to the mass among T Tauri stars ($<2\ M_{\odot}$) and the population of sources hosting disk decreases among high mass stars ($>2\ M_{\odot}$) suggesting rapid disk dispersal. Furthermore, we measured the disk color excess between the 2.2 μm K-band and 4.6 μm W2-band and although the color excess seems to decrease with decreasing mass, we require a large sample across a wider mass range to robustly correlate both. Our robust sample of spectroscopic brown dwarfs in the region are found to host a significant population of protoplanetary disks around them resulting in a non-negligible disk fraction for the substellar objects. We found that the lowest mass of objects with a disk are $\sim 20\ M_{\mathrm{Jup}}$. This supports the formation mechanism, which proposes the formation of brown dwarfs similar to low-mass stars.

Acknowledgements

We thank the anonymous referee for the constructive report, which has helped to improve the overall quality of the paper. Based on observations obtained with WIRCam, a joint project of CFHT, Taiwan, Korea, Canada and France, at the Canada-France-Hawaii Telescope (CFHT), which is operated by the National Research Council (NRC) of Canada, the Institut National des Sciences de l'Univers of the Centre National de la Recherche Scientifique of France, and the University of Hawaii. This work has made use of data from the European Space Agency (ESA) mission Gaia (https://www.cosmos.esa.int/gaia), processed by the Gaia Data Processing and Analysis Consortium (DPAC, https://www.cosmos.esa.int/web/gaia/dpac/consortium). Funding for the DPAC has been provided by national institutions, in particular, the institutions participating in the Gaia Multilateral Agreement. This publication makes use of data products from the Two Micron All Sky Survey, which is a joint project of the University of Massachusetts and the Infrared Processing and Analysis Center/California Institute of Technology, funded by the National Aeronautics and Space Administration and the National Science Foundation. This publication makes use of data products from the Wide-field Infrared Survey Explorer, which is a joint project of the University of California, Los Angeles and the Jet Propulsion Laboratory/California Institute of Technology, funded by the National Aeronautics and Space Administration. This work is based (in part) on observations made with the Spitzer Space Telescope, which was operated by the Jet Propulsion Laboratory, California Institute of Technology, under a contract with NASA. BD is thankful to the Center for Research, CHRIST (Deemed to be University), Bangalore, India. JJ acknowledges the financial support received through the DST-SERB grant SPG/2021/003850.

Appendix: Details of members in σ Orionis cluster

Table 2. Catalog of spectroscopically confirmed members of the σ Orionis cluster. The spectral type, effective temperature ($T_{\rm eff}$), bolometric luminosity and mass are taken from Damian *et al.* (2023). Column 6 and 7 are the YSO classifications reported for our sources in Hernández *et al.* (2007) and Koenig *et al.* (2015), respectively. Column 8 gives the SED slope (α) estimated in Section 5 and the corresponding YSO class is given in column 9.

Object ID	SpT	$T_{\rm eff}$ (K)	$\log(L_{\rm bol}/L_\odot)$	Mass ($M_\odot$)	Class (H07)	Class (K15)	α	Class (this work)
WBIS_053900.3-023705.9	M8	2539	−2.47	0.02	–	–	1.40	I
WBIS_053832.1-023243.1	M5	2880	−0.94	0.11	II	–	1.68	I
WBIS_053848.0-022714.2	M0	3770	0.42	0.50	II	II	−1.41	II
WBIS_053925.2-023822.0	K7	3970	−0.02	0.60	II	II	−0.92	II
WBIS_053831.4-023633.8	M3.5	3260	−0.46	0.20	II	II	−0.74	II
WBIS_053834.1-023637.5	M4	3160	−0.40	0.17	II	II	−1.16	II
WBIS_053827.3-024509.6	M0	3770	−0.30	0.50	II	II	−0.76	II
WBIS_053845.4-024159.6	M1	3630	−0.33	0.40	II	II	−1.02	II
WBIS_053831.6-023514.9	M0	3770	−0.12	0.50	II	II	−1.14	II
WBIS_053929.3-022721.0	M0	3770	−0.68	0.60	II	II	−0.52	II
WBIS_053827.5-023504.2	M3.5	3260	−0.77	0.20	II	II	−0.80	II
WBIS_053918.8-023053.2	K7	3970	−0.05	0.60	II	II	−1.11	II
WBIS_053907.6-023239.1	K5	4140	0.01	0.80	TD	TD	−0.92	II
WBIS_053908.8-023111.5	M3	3360	−0.81	0.30	CII	II	−1.04	II
WBIS_053859.2-023351.4	M2.5	3425	−0.82	0.30	II	II	−0.67	II
WBIS_053838.2-023638.5	K5	4140	0.06	0.80	III	–	−1.48	II
WBIS_053904.6-024149.2	M0	3770	−0.82	0.60	II	II	−0.74	II
WBIS_053823.3-022534.6	M2	3490	−1.06	0.40	II	II	−1.01	II
WBIS_053833.7-024414.3	K1	4920	0.57	0.86	II	II	−0.69	II
WBIS_053854.9-022858.3	M4.5	3020	−1.12	0.13	III	–	−0.94	II
WBIS_053806.7-023022.7	M1.5	3560	−0.26	0.40	II	II	−0.84	II
WBIS_053905.2-023300.5	–	–	–	–	III	–	−0.96	II
WBIS_053813.2-022608.8	M4.5	3020	−0.71	0.15	II	II	−1.35	II
WBIS_053817.8-024050.1	M5	2880	−0.91	0.11	II	II	−0.86	II
WBIS_053816.1-023804.9	M3.5	3260	−0.98	0.20	III	–	−0.92	II
WBIS_053911.5-023106.5	M0	3770	−0.32	0.50	II	II	−0.54	II
WBIS_053841.6-023028.9	M3	3360	−0.80	0.30	II	–	−0.71	II
WBIS_053820.5-023408.9	M4	3160	−0.79	0.17	II	II	−0.48	II
WBIS_053848.2-024400.8	–	–	–	–	II	II	−0.61	II
WBIS_053808.3-023556.2	M2.5	3425	−0.61	0.30	II	II	−0.91	II
WBIS_053835.9-024351.1	K0	5030	0.46	0.88	EV	TD	−1.61	II
WBIS_053903.0-024127.1	M2.5	3425	−0.67	0.30	II	II	−1.02	II
WBIS_053912.9-022453.5	M6	2860	−2.34	0.05	–	–	−0.75	II
WBIS_053850.6-024242.9	–	–	–	–	II	II	−1.18	II
WBIS_053838.9-022801.7	M5	2880	−1.75	0.06	III	–	–1.14	II
WBIS_053840.3-023018.5	M0	3770	−0.12	0.50	II	II	−1.12	II
WBIS_053826.8-023846.1	M3.5	3260	−1.20	0.20	II	II	−1.29	II
WBIS_053915.1-024047.6	M3.5	3260	−1.37	0.20	III	–	−1.42	II
WBIS_053839.8-023220.3	M7	2683	−1.56	0.04	II	–	−1.21	II
WBIS_053855.4-024120.8	M5.5	2920	−1.72	0.07	II	–	−0.79	II
WBIS_053901.9-023502.8	M4	3160	−1.40	0.17	II	II	−0.85	II
WBIS_053835.4-022522.2	M6	2860	−1.50	0.06	III	–	−1.49	II
WBIS_053825.4-024241.2	M7	2683	−1.59	0.04	II	–	−1.30	II
WBIS_053913.1-023750.9	M6	2860	−1.70	0.06	II	–	−1.15	II
WBIS_053839.0-024532.1	M2.5	3425	−0.77	0.30	II	II	−1.54	II

Table 2. Continued.

Object ID	SpT	$T_{\rm eff}$ (K)	$\log(L_{\rm bol}/L_{\odot})$	Mass ($M_{\odot}$)	Class (H07)	Class (K15)	α	Class (this work)
WBIS_053840.5-023327.6	M5	2880	−0.83	0.11	II	II	−1.44	II
WBIS_053849.3-022357.5	M3.5	3260	−1.28	0.20	II	II	−1.49	II
WBIS_053848.1-022853.6	M5.5	2920	−1.39	0.08	II	–	−1.44	II
WBIS_053832.4-022957.3	M6.5	2815	−1.79	0.05	III	–	−1.11	II
WBIS_053926.3-022837.7	M5	2880	−1.02	0.10	II	II	−1.41	II
WBIS_053926.9-023656.1	M6.5	2815	−1.80	0.05	II	–	−1.29	II
WBIS_053833.9-024507.8	–	–	–	–	II	II	−1.42	II
WBIS_053843.9-023706.9	M5.5	2920	−0.85	0.11	II	II	−1.40	II
WBIS_053844.2-024019.7	K5	4140	−0.02	0.80	II	II	−0.98	II
WBIS_053847.2-023436.9	M4	3160	−0.74	0.17	II	II	−1.28	II
WBIS_053854.9-024033.8	M8	2539	−1.90	0.02	II	–	−1.20	II
WBIS_053807.1-024321.1	M7	2683	−2.43	0.03	–	–	0.09	flat
WBIS_053925.6-023843.7	–	–	–	–	–	II	0.22	flat
WBIS_053812.6-023637.7	M7	2683	−1.95	0.03	II	–	−0.26	flat
WBIS_053923.4-024057.5	M7.5	2611	−2.20	0.02	–	–	−1.63	III
WBIS_053918.1-022928.5	K0	5030	0.35	0.88	DD	–	−1.92	III
WBIS_053847.5-022712.0	M5	2880	−0.65	0.13	EV	–	−2.66	III
WBIS_053834.8-023415.7	A1	9300	1.49	2.05	III	–	−3.02	III
WBIS_053838.5-023455.0	K2	4760	0.64	0.82	EV	–	−2.47	III
WBIS_053834.2-023416.0	B7	14000	2.48	3.92	III	–	−2.98	III
WBIS_053901.5-023856.4	B5	15700	2.77	4.70	III	–	−2.96	III
WBIS_053841.3-023722.6	K5	4140	−0.06	0.80	III	–	−2.68	III
WBIS_053844.2-023233.6	K4	4330	0.20	1.00	III	–	−2.76	III
WBIS_053832.8-023539.2	M0	3770	−0.14	0.50	III	–	−2.66	III
WBIS_053853.4-023323.0	K3	4550	0.34	1.20	III	–	−2.76	III
WBIS_053925.6-023404.2	M5.5	2920	−0.93	0.11	III	–	−2.18	III
WBIS_053835.9-023043.3	K4	4330	0.05	1.00	III	–	−2.68	III
WBIS_053843.6-023325.4	M1	3630	−0.22	0.4	III	–	−2.46	III
WBIS_053921.0-023033.5	–	–	–	–	III	–	−2.06	III
WBIS_053842.3-023714.8	M0	3770	−0.23	0.50	II	II	−1.73	III
WBIS_053849.2-024125.1	M6	2860	−0.32	0.13	III	–	−2.66	III
WBIS_053900.5-023939.0	G3.5	5680	0.05	1.10	–	–	−2.80	III
WBIS_053926.8-024258.3	–	–	–	–	EV	II	−1.73	III
WBIS_053839.7-024019.7	M3.5	3260	−1.06	0.20	III	–	−2.18	III
WBIS_053902.8-022955.8	M4	3160	−0.74	0.17	III	–	−2.67	III
WBIS_053853.2-024352.6	M1	3630	−0.43	0.40	III	–	−2.63	III
WBIS_053924.4-023401.3	M2	3490	−0.75	0.30	III	–	−2.21	III
WBIS_053905.4-023230.3	K5	4140	−0.09	0.80	III	–	−2.77	III
WBIS_053807.8-023130.7	K3	4550	0.36	1.20	III	–	−2.93	III
WBIS_053901.2-023638.8	–	–	–	–	III	–	−2.36	III
WBIS_053833.4-023617.6	M2.5	3425	−0.39	0.30	III	–	−2.85	III
WBIS_053911.6-023602.8	K5	4140	−0.12	0.80	III	–	−2.60	III
WBIS_053827.5-024332.5	A2	8800	1.38	1.98	III	–	−2.90	III
WBIS_053932.6-023944.0	K5	4140	0.20	0.70	III	–	−2.86	III
WBIS_053836.5-023312.7	B5	15700	2.77	4.70	III	–	−2.94	III
WBIS_053917.2-022543.3	M1.5	3560	−0.67	0.40	III	–	−2.45	III
WBIS_053835.5-023151.6	K4	4330	0.03	1.00	III	–	−2.84	III
WBIS_053843.3-023200.8	M5	2880	−0.71	0.13	III	–	−2.44	III
WBIS_053850.4-022647.7	M3.5	3260	−0.68	0.20	EV	–	−2.32	III
WBIS_053912.3-023006.4	M5	2880	−0.77	0.13	III	–	−2.57	III

Table 2. Continued.

Object ID	SpT	$T_{\rm eff}$ (K)	$\log(L_{\rm bol}/L_\odot)$	Mass ($M_\odot$)	Class (H07)	Class (K15)	α	Class (this work)
WBIS_053847.7-023037.4	M5.5	2920	−1.02	0.11	III	–	−2.32	III
WBIS_053827.7-024300.9	M3	3360	−0.45	0.30	III	–	−2.79	III
WBIS_053920.4-022736.8	M2	3490	−0.42	0.30	III	–	−2.56	III
WBIS_053925.3-023143.6	G3.5	5680	−0.33	1.0	III	–	−2.76	III
WBIS_053907.6-022823.3	M3	3360	−0.77	0.30	III	–	−2.48	III
WBIS_053922.9-023333.0	M2	3490	−0.73	0.30	III	–	−2.40	III
WBIS_053914.5-022833.3	M3.5	3260	−0.91	0.20	III	–	−2.12	III
WBIS_053908.2-023228.4	M5	2880	−1.13	0.09	III	–	−2.02	III
WBIS_053859.5-024508.0	F3	6660	0.37	1.4	–	–	−2.90	III
WBIS_053913.5-023739.0	M4	3160	−0.98	0.17	III	–	−1.97	III
WBIS_053915.8-023650.7	M4	3160	−0.93	0.17	II	II	−1.61	III
WBIS_053926.5-022615.4	M1.5	3560	−0.90	0.40	III	–	−2.20	III
WBIS_053823.1-023649.3	M4.5	3020	−1.10	0.13	II	II	−1.75	III
WBIS_053834.6-024108.8	M2	3490	−0.82	0.40	II	II	−1.70	III
WBIS_053834.3-023500.1	K5	4140	0.04	0.80	III	–	−2.84	III
WBIS_053829.1-023602.7	M1.5	3560	−0.67	0.40	III	–	−2.69	III
WBIS_053845.3-023729.3	M5.5	2920	−0.99	0.11	II	–	−1.80	III
WBIS_053849.9-024122.8	M3	3360	−0.78	0.30	III	–	−2.48	III
WBIS_053920.2-023825.9	M5.5	2920	−1.07	0.10	III	–	−2.42	III
WBIS_053826.2-024041.3	M4.5	3020	−1.53	0.10	III	–	−2.46	III
WBIS_053814.7-024015.2	L1	2102	−2.42	0.007	–	–	−2.56	III
WBIS_053915.8-023826.3	M4.5	3020	−1.58	0.10	–	–	−2.23	III
WBIS_053911.8-022741.0	M4.5	3020	−1.03	0.13	III	–	−2.73	III
WBIS_053851.5-023620.6	K5	4140	−0.60	0.80	EV	–	−2.56	III
WBIS_053825.7-023121.7	M3.5	3260	−1.42	0.20	III	–	−2.51	III
WBIS_053805.5-023557.1	M4.5	3020	−1.73	0.09	II	–	−2.03	III
WBIS_053849.2-023822.3	K7	3970	−0.05	0.60	III	–	−2.85	III
WBIS_053817.4-024024.2	M6	2860	−1.56	0.06	–	–	−2.32	III
WBIS_053829.6-022514.2	M4	3160	−1.51	0.15	III	–	−2.43	III
WBIS_053848.7-023616.3	M1.5	3560	−0.60	0.40	III	–	−2.91	III
WBIS_053850.0-023735.5	M5.5	2920	−0.89	0.11	III	–	−2.55	III
WBIS_053846.0-024523.1	M5	2880	−1.05	0.10	III	–	−2.54	III
WBIS_053823.3-024414.2	M4	3160	−0.99	0.17	III	–	−2.72	III
WBIS_053821.4-023336.3	M6	2860	−1.77	0.06	III	–	−2.49	III
WBIS_053823.5-024131.7	M4.5	3020	−0.95	0.13	III	–	−2.68	III
WBIS_053818.3-023538.6	M7	2683	−1.67	0.04	III	–	−2.26	III
WBIS_053852.6-023215.5	M6.5	2815	−2.14	0.04	–	–	−2.44	III
WBIS_053820.2-023801.6	M4.5	3020	−0.71	0.15	III	–	−2.64	III
WBIS_053813.2-022407.5	M5.5	2920	−1.28	0.09	III	–	−2.47	III
WBIS_053853.8-024458.8	M6	2860	−1.83	0.05	–	–	−2.49	III
WBIS_053911.4-023332.8	M5	2880	−1.41	0.07	III	–	−2.53	III
WBIS_053849.7-023452.7	M5	2880	−0.88	0.11	II	II	−2.08	III
WBIS_053850.8-023626.8	M3	3360	−0.88	0.30	III	–	−2.47	III
WBIS_053908.9-023957.9	M7	2683	−1.43	0.05	III	–	−2.29	III
WBIS_053838.6-024155.9	M5.5	2920	−1.44	0.075	III	–	−2.50	III
WBIS_053851.7-023603.4	M6	2860	−0.87	0.11	III	–	−2.52	III
WBIS_053836.9-023643.3	M4.5	3020	−0.88	0.13	III	–	−2.62	III
WBIS_053847.2-023540.6	B2	20600	3.43	7.30	III	–	−3.03	III
WBIS_053904.5-023835.3	M6	2860	−1.53	0.06	III	–	−2.37	III
WBIS_053908.1-022844.8	M4	3160	−1.22	0.17	EV	–	−2.43	III

Table 2. Continued.

Object ID	SpT	$T_{\rm eff}$ (K)	$\log(L_{\rm bol}/L_\odot)$	Mass ($M_\odot$)	Class (H07)	Class (K15)	α	Class (this work)
WBIS_053844.8-023600.2	O9.5	31900	4.72	18.70	–	–	–	–
WBIS_053841.5-023552.3	M6	2860	−1.25	0.08	–	–	–	–
WBIS_053844.1-023606.3	A2	8800	1.38	1.98	–	–	–	–
WBIS_053845.3-023541.2	M5.5	2920	−1.09	0.10	–	–	–	–
WBIS_053835.3-023313.1	M5.5	2920	−1.21	0.09	–	–	–	–
WBIS_053835.8-023313.4	M5.5	2920	−1.14	0.10	–	–	–	–
WBIS_053842.4-023604.5	M6	2860	−1.30	0.075	–	–	–	–
WBIS_053844.5-024037.7	M6.5	2815	−1.54	0.05	–	–	–	–
WBIS_053913.8-023145.6	M8.5	2467	−2.57	0.015	–	–	–	–
WBIS_053910.8-023714.6	M9	2394	−2.61	0.01	–	–	–	–
WBIS_053903.6-022536.7	L0	2248	−2.93	0.01	–	–	–	–
WBIS_053852.7-022843.7	L0	2248	−3.47	0.04	–	–	–	–
WBIS_053829.5-022937.0	L1	2102	−3.01	0.008	–	–	–	–
WBIS_053857.5-022905.5	L1	2102	−3.08	0.009	–	–	–	–
WBIS_053803.2-022656.7	L1	2102	−3.20	0.01	–	–	–	–
WBIS_053826.1-022305.0	L3.5	1756	−3.41	0.005	–	–	–	–
WBIS_053839.2-022805.8	L5	1581	−3.20	0.004	–	–	–	–
WBIS_053844.5-024030.5	–	–	–	–	–	–	–	–
WBIS_053848.3-023641.0	M4.5	3020	−0.63	0.15	–	–	–	–
WBIS_053841.4-023644.5	M2	3490	−0.81	0.40	–	–	–	–
WBIS_053847.5-023524.9	M1	3630	−0.23	0.40	–	–	–	–
WBIS_053846.8-023643.6	M5	2880	−0.98	0.10	–	–	–	–
WBIS_053843.0-023614.6	M1	3630	−0.30	0.40	–	–	–	–
WBIS_053845.6-023559.0	B2	20600	3.43	7.30	–	–	–	–
WBIS_053903.2-023020.0	M9	2394	−2.47	0.01	–	–	–	–

References

Allers K. N., Liu M. C. 2020, PASP, 132, 104401

Andre P., Ward-Thompson D., Barsony M. 2000, prpl.conf., 59

André P., Ward-Thompson D., Greaves J. 2012, Sci., 337, 69

Andrews S. M. 2020, ARA&A, 58, 483

Ansdell M., Williams J. P., Manara C. F., *et al.* 2017, AJ, 153, 240

Baraffe I., Chabrier G., Barman T. S., Allard F., Hauschildt P. H. 2003, A&A, 402, 701

Baraffe I., Homeier D., Allard F., Chabrier G. 2015, A&A, 577, A42

Béjar V. J. S., Zapatero Osorio M. R., Rebolo R. 2004, AN, 325, 705

Bouvier J., Alencar S. H. P., Harries T. J., Johns-Krull C. M., Romanova M. M. 2007, prpl.conf., 479

Caballero J. A., Béjar V. J. S., Rebolo R., *et al.* 2007, A&A, 470, 903

Calvet N., Muzerolle J., Briceño C., *et al.* 2004, AJ, 128, 1294

Cardelli J. A., Clayton G. C., Mathis J. S. 1989, ApJ, 345, 245

Currie T., Lada C. J., Plavchan P., *et al.* 2009, ApJ, 698, 1

Cutri R. M., Skrutskie M. F., van Dyk S., *et al.* 2003, yCat, II/246

Cutri R. M., *et al.* 2012, yCat, II/311

Dahm S. E., Hillenbrand L. A. 2007, AJ, 133, 2072

Damian B., Jose J., Samal M. R., *et al.* 2021, MNRAS, 504, 2557

Damian B., Jose J., Biller B. *et al.* 2023, ApJ, 951, 139

Das S. R., Jose J., Samal M. R., Zhang S., Panwar N. 2021, MNRAS, 500, 3123

Das S. R., Gupta S., Prakash P., Samal M., Jose J. 2023, ApJ, 948, 7

Dubber S., Biller B., Allers K., *et al.* 2021, MNRAS, 505, 4215

Esplin T. L., Luhman K. L. 2017, AJ, 154, 134

Esplin T. L., Luhman K. L. 2022, AJ, 163, 64

Fabricius C., Luri X., Arenou F., *et al.* 2021, A&A, 649, A5

Filippazzo J. C., Rice E. L., Faherty J., *et al.* 2015, ApJ, 810, 158

Frank A., Ray T. P., Cabrit S., *et al.* 2014, prpl.conf., 451

Furlan E., Hartmann L., Calvet N., *et al.* 2006, ApJS, 165, 568

Gaia Collaboration 2022, yCat, I/355

Greene T. P., Wilking B. A., Andre P., Young E. T., Lada C. J. 1994, ApJ, 434, 614

Gupta S., Jose J., More S., *et al*. 2021, MNRAS, 508, 3388

Guzmán-Díaz J., Mendigutía I., Montesinos B., *et al*. 2021, A&A, 650, A182

Han C., Jung Y. K., Udalski A., *et al*. 2013, ApJ, 778, 38

Hartigan P., Edwards S., Ghandour L. 1995, ApJ, 452, 736

Hartmann L. 2009, apsf.book

Hartmann L., Herczeg G., Calvet N. 2016, ARA&A, 54, 135

Herczeg G. J., Hillenbrand L. A. 2014, ApJ, 786, 97

Hernández J., Calvet N, Briceño C., *et al*. 2007, ApJ, 671, 1784

Hernández J., Hartmann L., Megeath T., *et al*. 2007, ApJ, 662, 1067

Hillenbrand L. A., Strom S. E., Calvet N., *et al*. 1998, AJ, 116, 1816

Johnson J. A., Aller K. M., Howard A. W., Crepp J. R. 2010, PASP, 122, 905

Jose J., Biller B. A., Albert L., *et al*. 2020, ApJ, 892, 122

Koenig X. P., Leisawitz D. T. 2014, ApJ, 791, 131

Koenig X., Hillenbrand L. A., Padgett D. L., DeFelippis D. 2015, AJ, 150, 100

Kordopatis G., Schultheis M., McMillan P. J., *et al*. 2023, A&A, 669, A104

Lada C. J. 1987, IAUS, 115, 1

Lada E. A., Lada C. J. 1995, AJ, 109, 1682

Lada C. J., Muench A. A., Luhman K. L., *et al*. 2006, AJ, 131, 1574

Lalchand B., Chen W.-P., Biller B. A., *et al*. 2022, AJ, 164, 125

Luhman K. L., Lada C. J., Hartmann L., *et al*. 2005, ApJL, 631, L69

Luhman K. L., Hernández J., Downes J. J., Hartmann L., Briceño C. 2008, ApJ, 688, 362

Luhman K. L. 2012, ARA&A, 50, 65

Manara C. F., Frasca A., Venuti L., *et al*. 2021, A&A, 650, A196

Meyer M. R., Backman D. E., Weinberger A. J., Wyatt M. C. 2007, prpl.conf., 573

Michel A., van der Marel N., Matthews B. C. 2021, ApJ, 921, 72

Miotello A., Kamp I., Birnstiel T., Cleeves L. I., Kataoka A. 2022, arXiv, arXiv:2203.09818

Monteiro H., Dias W. S., Moitinho A., *et al*. 2020, MNRAS, 499, 1874

Muench A. A., Alves J., Lada C. J., Lada E. A. 2001, ApJL, 558, L51

Natta A., Testi L., Comerón F., *et al*. 2002, A&A, 393, 597

Padoan P., Nordlund Å. 2002, ApJ, 576, 870

Panwar N., Samal M. R., Pandey A. K., *et al*. 2017, MNRAS, 468, 2684

Pascucci I., Cabrit S., Edwards S., *et al*. 2022, arXiv, arXiv:2203.10068

Pecaut M. J., Mamajek E. E. 2013, ApJS, 208, 9

Peña Ramírez K., Béjar V. J. S., Zapatero Osorio M. R., Petr-Gotzens M. G., Martín E. L. 2012, ApJ, 754, 30

Penoyre Z., Belokurov V., Evans N. W. 2022, MNRAS, 513, 5270

Puget P., Stadler E., Doyon R., *et al*. 2004, SPIE, 5492, 978

Rayner J. T., Toomey D. W., Onaka P. M., *et al*. 2003, PASP, 115, 362

Reipurth B., Clarke C. 2001, AJ, 122, 432

Ribas Á., Bouy H., Merín B. 2015, A&A, 576, A52

Rilinger A. M., Espaillat C. C. 2021, ApJ, 921, 182

Sherry W. H., Walter F. M., Wolk S. J., Adams N. R. 2008, AJ, 135, 1616

Scholz A., Jayawardhana R. 2008, ApJL, 672, L49

Scholz A., Muzic K., Jayawardhana R., Almendros-Abad V., Wilson I. 2023, arXiv, arXiv:2303.12451

Shvartzvald Y., Yee J. C., Calchi Novati S., *et al*. 2017, ApJL, 840, L3

Spitzer Science Center (SSC), Infrared Science Archive (IRSA) 2021, yCat, II/368

Stamatellos D., Maury A., Whitworth A., André P. 2011, MNRAS, 413, 1787

Stoop M., Kaper L., de Koter A., *et al*. 2023, A&A, 670, A108

Wang S., Chen X. 2019, ApJ, 877, 116

Williams J. P., Cieza L. A. 2011, ARA&A, 49, 67

Winter A. J., Clarke C. J., Rosotti G., *et al*. 2018, MNRAS, 478, 2700

Whitworth A. P., Zinnecker H. 2004, A&A, 427, 299

Yao Y., Meyer M. R., Covey K. R., Tan J. C., Da Rio N. 2018, ApJ, 869, 72